Topological defects in two-dimensional liquid crystals confined by a box

Xiaomei Yao,[1,2] Hui Zhang,[1,*] and Jeff Z. Y. Chen[3,†]
[1]*School of Mathematical Sciences, Beijing Normal University, Beijing 100875, People's Republic of China*
[2]*School of Chemistry, Beihang University, Beijing 100191, People's Republic of China*
[3]*Department of Physics and Astronomy, University of Waterloo, Waterloo, Ontario, Canada, N2L 3G1*

(Received 9 January 2018; published 30 May 2018)

When a spatially uniform system that displays a liquid-crystal ordering on a two-dimensional surface is confined inside a rectangular box, the liquid crystal direction field develops inhomogeneous textures accompanied by topological defects because of the geometric frustrations. We show that the rich variety of nematic textures and defect patterns found in recent experimental and theoretical studies can be classified by the solutions of the rather fundamental, extended Onsager model. This is critically examined based on the determined free energies of different defect states, as functions of a few relevant, dimensionless geometric parameters.

DOI: 10.1103/PhysRevE.97.052707

I. INTRODUCTION

Nature has it that some physical systems of vastly different scales and composed of different materials present the same phenomena, which in turn can be classified by a single physical picture. The topic of anisotropically shaped particles confined on a surface with a boundary enclosing them is an excellent example. The word "particles" needs to be interpreted generally. These could be a thin layer of liquid-crystal molecules confined in a micron-sized well [1], aqueous suspensions of actin filaments [2] and linearly shaped virus [3] confined in a microchamber, and micron-sized colloidal silica rods [4] or visible-range granular rods [5,6] flatly laid on a leveled bed confined by a box of approximately one order of magnitude larger. In an ideal bulk state without a boundary, the anisotropic nature of these particles drives them into the formation of a directionally ordered but spatially homogeneous liquid state known as the nematic phase [7] under sufficiently high particle-number density. A uniform orientational direction, along the common nematic director, can be identified.

The confinement boundary, of any geometric shapes, however, disrupts the otherwise uniform, directionalized pattern. The frustrated director field begins to display a range of different configurations and the orientational pattern now shows topological defects. The most stable defect states within the rectangular confinement, diagonal (D), X-shaped (X), and long-axis (L) states, are showcased in Fig. 1. While understanding of topological defects in liquid crystals is a research field that spans over other types of geometries and dimensions [7–11], here we focus on two-dimensional (2D) systems with a simple rectangular confinement boundary. We demonstrate that these simple systems display all essential features of the more complicated liquid-crystal confinement problems and that the orientational patterns observed in the above experiments can be qualitatively accounted for by extending a fundamental statistical physics model known as the Onsager theory [12].

On the application side, the defect structures, such as those in Fig. 1, can produce different, polarized optical properties. Most 2D defect structures discussed below correspond to free-energy minima partitioned from each other by barriers. Switching between different defect states could be achieved by an external field that lowers the energy barrier and biased to one of the states. The possible coexistence of these multiple states in miniaturized, confining cells is a desirable feature [1] for liquid-crystal display industries [13], among other techniques that produce multistable liquid crystal devices [14–16].

There are only three most relevant, dimensionless parameters that control the type of resulting nematic patterns in these systems. The aspect ratio of a confining rectangle b/a, where a and b are the short- and long-side lengths, and the box-rod size ratio a/L, where L is the length of a rodlike particle, define the confinement geometry. In a system consisting of n sterically repelling particles, the reduced number of particles per unit area, $L^2\rho \equiv L^2 n/ab$, determines the degree of orientational ordering and hence the type of nematic patterns as well. Originally, Onsager proposed a free-energy model for the bulk properties of the isotropic-nematic transition in three dimensions [12]. The model was later extended to include the positional dependence of the distribution function [17–23]. For the current problem, the free energy must be minimized with respect to the particle configurations, which produces a solution for the distribution function $f(x,y,\theta)$ at given $[L^2\rho, a/L, a/b]$, where x,y are the Cartesian coordinates to describe the location of a point in the box and θ is an angle to describe the particle's axial direction from the x axis [24]. Section II summarizes this approach.

In a complex free-energy landscape, a single solution corresponds to a local ("metastable") or global ("stable") minimum. Depending on the physical conditions, an observed structure in a theoretical or real experimental system can correspond to the global minimum or can be trapped in a local minimum if the free-energy barrier between these is high. Section III A further explains these concepts.

Multiple defect patterns have been found in this work. The results are organized in two subsections. In Sec. III B, we consider those for fixed $L^2\rho = 10$, which is in a relatively deep

*hzhang@bnu.edu.cn
†jeffchen@uwaterloo.ca

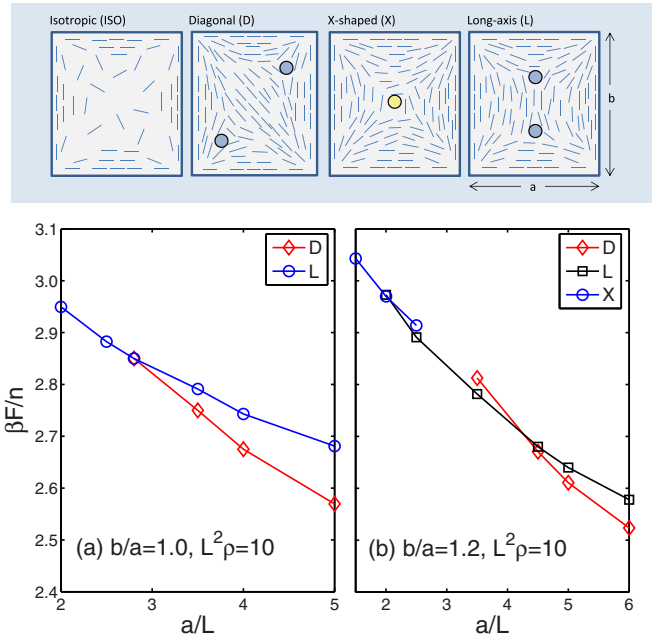

FIG. 1. Typical nematic defect states (top) and their free-energy (per molecule) branches as functions of a/L for fixed (a) $[b/a, L^2\rho] = [1,10]$ and (b) $[1.2,10]$. Defect points of winding numbers $-1/2$ (blue) and -1 (yellow) are seen in the diagonal, long-axis, and X-shaped states. The crossing of these branches yields a phase boundary for the transition between the two involved states.

nematic state. Most experimental work (mentioned above) and computer simulations [25–30] are conducted in well-formed nematic state. It is here we present a discussion of our findings with other work.

Other theoretical tools, such as the Landau–de Gennes and Oseen-Frank models, were used to study the current problem. These models contain phenomenological parameters that cannot be easily identified with, for example, a/L and $L^2\rho$ [1,3,6,30,31]. One commonly used approximation in solving these models has been the one-elastic-modulus approximation, which is only valid near the isotropic-nematic transition boundary. To compare with previous theoretical results, as our second set of calculations, we let $L^2\rho = 6$, near the transition boundary. Some of the defect patterns described in Sec. III B are comparable to those found in Ref. [30] and some are new. The defect patterns predicted in this subsection could be observed by future experiments.

In general, how do we classify the 2D nematic defect patterns within a line boundary? This is a question that goes beyond the rectangular confinement. In Sec. III D we classify the confinement types by the number of confinement boundary corners n and present a general formula for the total winding number $W(n)$ of a given type. All defect patterns discussed in this work follow the expect rule for $n = 4$.

The extended Onsager theory can be presented as a self-consistent field theory of wormlike-chain polymers with infinite rigidity. This and the computer algorithm that is used to solve the theory numerically, are presented in the Appendices.

II. METHODS

A. Extended Onsager model

Of the central focus is the density distribution function $\rho_c(\mathbf{r},\mathbf{u})$ which characterizes the probability density of finding the centers of mass of the rodlike molecules at a spatial position specified by the vector $\mathbf{r}$ with the condition that the rods are pointing at the direction specified by a unit vector $\mathbf{u}$. Here we assume that $\rho_c(\mathbf{r},\mathbf{u})$ is normalized to n. For a given, unknown distribution $\rho_c(\mathbf{r},\mathbf{u})$, accurate to the second-virial coefficient [32], the extended Onsager model states that the free energy of the system is a functional [7,12,33],

$$\beta F = \int \rho_c(\mathbf{r},\mathbf{u}) \ln[L^2\rho_c(\mathbf{r},\mathbf{u})] d\mathbf{r}d\mathbf{u} + \frac{1}{2}\int \rho_c(\mathbf{r},\mathbf{u}) w(\mathbf{r},\mathbf{u};\mathbf{r}',\mathbf{u}') \rho_c(\mathbf{r}',\mathbf{u}')\, d\mathbf{r}d\mathbf{u}d\mathbf{r}'d\mathbf{u}', \tag{1}$$

where $\beta = 1/k_BT$, with k_B being the Boltzmann constant and T the temperature. To obtain the stable or metastable configurational properties, the free energy is to be minimized with respect to $\rho_c(\mathbf{r},\mathbf{u})$ with the appropriate hard-wall boundary conditions. The free energy includes two terms. The first term is ideal-gas-like, containing both translational and orientational entropies of a spatially inhomogeneous and orientationally ordered gas of rodlike molecules. The kernel function $w(\mathbf{r},\mathbf{u};\mathbf{r}',\mathbf{u}')$ in the second term describes the interaction between two rods respectively having the coordinates $(\mathbf{r},\mathbf{u})$ and $(\mathbf{r}',\mathbf{u}')$. The two terms compete with each other as one prefers isotropic state and the other nematic state.

The actual numerical calculation to minimize the free energy was carried out by using the mathematically equivalent self-consistent field theory [24,34]. Appendix A summarizes the main formalism.

B. Visualization of the nematic structures

The calculated physical properties are based on the distribution function of segments on a rodlike molecule, $f(\mathbf{r},\mathbf{u})$. It is related to the center-of-mass distribution function $\rho_c(\mathbf{r},\mathbf{u})$ by

$$f(\mathbf{r},\mathbf{u}) = \frac{ab}{n}\int_0^1 \rho_c\left[\mathbf{r} - \mathbf{u}L\left(s - \frac{1}{2}\right),\mathbf{u}\right] ds, \tag{2}$$

where we trace back along the path of a rodlike molecule to the rod center. The integrant represents the probability density of finding the segment labeled by s on the rodlike molecule to appear at a location with the coordinate $\mathbf{r}$. The path-averaged $f(\mathbf{r},\mathbf{u})$ is the probability density of finding *any segments*, regardless of its label s, to appear at $\mathbf{r}$. With this definition $f(\mathbf{r},\mathbf{u})$ is dimensionless and normalized to the box area ab. In 2D, $f(\mathbf{r},\mathbf{u})$ is expressed by $f(x,y;\theta)$, where x,y are the Cartesian coordinates along the two perpendicular sides of a rectangle and θ is the angle between $\mathbf{u}$ and the x axis. Here a number of physical quantities are introduced to illustrate the nature of the three-variable function $f(x,y;\theta)$.

The density variation is reflected by the function

$$\phi(x,y) = \int_0^{2\pi} f(x,y,\theta) d\theta, \tag{3}$$

where the θ dependence of the distribution function is averaged out. In the bulk isotropic and nematic states, this function is identically constant (=1). In the current system, the nematic defect locations normally accompany a low $\phi(x,y)$.

On a 2D surface, to measure the orientational ordering, we define the orientational order parameter tensor

$$\mathsf{Q}(x,y) = \frac{1}{2}\begin{bmatrix} S(x,y) & T(x,y) \\ T(x,y) & -S(x,y) \end{bmatrix}, \tag{4}$$

where the two elements are

$$S(x,y) = \frac{\int_0^{2\pi} d\theta \cos(2\theta) f(x,y,\theta)}{\phi(x,y)}, \tag{5}$$

$$T(x,y) = \frac{\int_0^{2\pi} d\theta \sin(2\theta) f(x,y,\theta)}{\phi(x,y)}. \tag{6}$$

Respectively, S and T characterize the ordering of the rodlike molecules along the x axis and the direction that makes a $\pi/4$ angle with respect to the x axis. Note that both S and T defined here have been divided by $\phi(x,y)$, whereas similar quantities studied in Ref. [24] were directly the integrals in the numerators.

Based on this definition, the main order parameter measured from a local nematic director $\mathbf{n}(x,y)$ is found from the positive eigenvalue of the Q tensor,

$$\Lambda(x,y) = \sqrt{S^2(x,y) + T^2(x,y)}. \tag{7}$$

The nematic-director field itself is projected on the Cartesian axes by

$$\mathbf{n}(x,y) = \hat{x}\cos\theta_0(x,y) + \hat{y}\sin\theta_0(x,y), \tag{8}$$

where θ_0 is determined from

$$\cos\theta_0(x,y) = \frac{1}{2}\left[1 + \frac{S(x,y)}{\Lambda(x,y)}\right]. \tag{9}$$

The location where $\Lambda = 0$ is considered as a defect point and hence $\mathbf{n}$ cannot be defined.

In a typical optical experiment, to image the possible defect pattern, a liquid-crystal cell is placed between two crossed polarizers. To model the defect pattern seen by the experiments, here we assume that the first polarizer makes an angle α with respect to the x axis. After the light passes the liquid-crystal cell, the electric field E makes a projection $E\cos(\alpha-\theta)$ after been screened by those molecular segments oriented in the θ direction. Another projection of $\sin(\alpha-\theta)$ along the axis of the second polarizer makes the final outcome of the light intensity proportional to

$$I_\alpha(x,y) = \frac{1}{4}\int_0^{2\pi} d\theta [\sin(2\theta - 2\alpha)]^2 f(x,y;\theta). \tag{10}$$

The average is performed locally with respect to the molecular orientation θ.

III. RESULTS AND DISCUSSION

A. Free energy and phase diagrams

The relative stability of a defect state over the other can be assessed by examining the free-energy differences between these states. For example, each data point in Fig. 1(a) represents the free energy per particle, calculated after minimization is performed with respect to the probability density distribution for a fixed $b/a = 1$ and $L^2\rho = 10$. The interpolation of the calculated data indicates that a first-order phase transition takes place at $a/L \approx 2.8$, where, beyond this point, D has a lower free energy. This leads to the phase boundary in the phase diagram, Fig. 2(a), at $[a/L, L^2\rho] = [2.8, 10]$. Calculations for other values of $L^2\rho$ give rise to the entire phase boundary curve for the X-D transition.

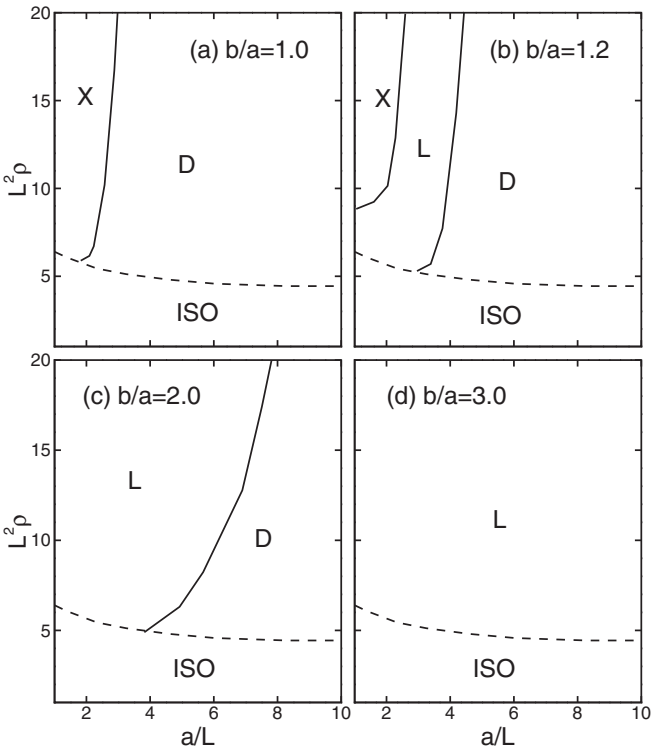

FIG. 2. Phase diagrams in terms of a/L and $L^2\rho$ for four given aspect ratios, $b/a = 1, 1.2, 2$, and 3. A second-order phase transition curve (dashed) separates the parameter space into ordered and isotropic (ISO) states.

In another example, for a system with fixed $b/a = 1.2$ and $L^2\rho = 10$, by changing a/L we obtain three free-energy branches corresponding to X, L, and D, which are displayed in Fig. 1(b). The first crossing point at $L^2\rho \approx 2.0$ determines the X-L phase boundary and the second at $L^2\rho \approx 4.1$ the L-D phase boundary. Within this two points, both D and X are metastable.

Our system has three parameters, $[L^2\rho, b/a, a/L]$. A complete phase diagram is hence dependent on three system parameters. Figure 2 is a series of two-dimensional phase diagrams with fixed values of the aspect ratio b/a. The phase diagram shows the parameter space where the D, X, or L states have the lowest free energy.

The Onsager model ignores all fluctuation effects and hence is at a mean-field level. As such, when it is used to model the isotropic-nematic phase transition of rodlike molecules in 2D, it predicts a second-order transition density [21,35,36],

$$L^2\rho^* = 3\pi/2, \tag{11}$$

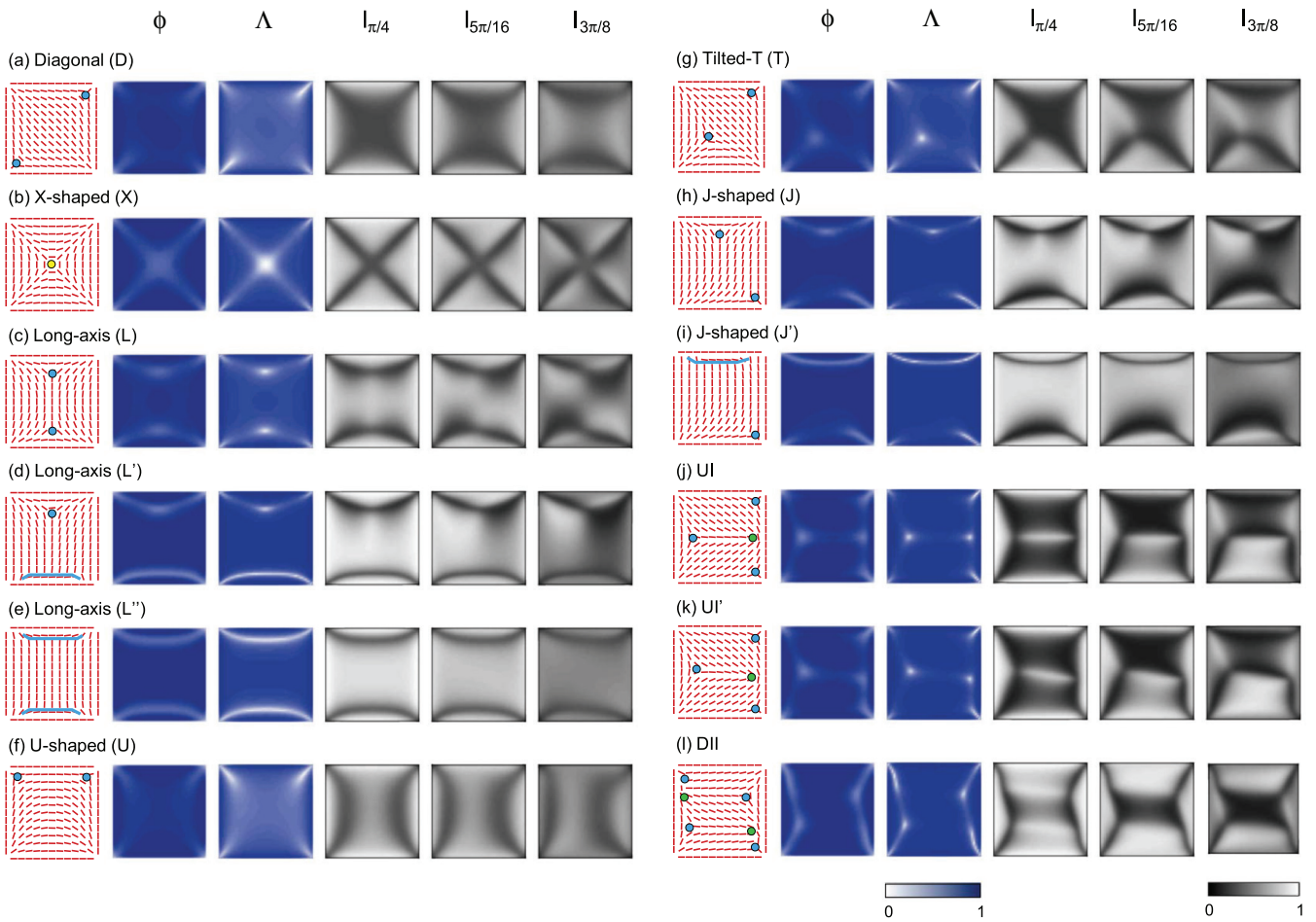

FIG. 3. Nematic defect structures found from the solutions to the extended Onsager model for $b/a = 1$. Every structure is visualized by six methods: nematic-director field, fluid density variation ϕ, main-axis orientational order parameter Λ, and three gray-scale crossed-polarizer images calculated according to (10) for $\alpha = \pi/4, 5\pi/16$, and $3\pi/8$. The reduced parameters used to produce these structures are $[L^2\rho, a/L] = [10.0, 8.0]$ for (a) and (f) and $[10.0, 10.0]$ for (b)–(e) and (j)–(l). The color scale used for columns 2 and 3 is indicated by the white-blue color bar and the grayscale used for all I_α plots by the black-white gray bar. The blue, yellow, and green circles label the defect locations of $-1/2$, -1, and $+1/2$ winding numbers, respectively. The three gray-scale images of D and U states closely match the real crossed-polarizer images of a liquid crystal confined in 80-μm square cells, reported in Ref. [1].

above which the nematic state is stable and below which the isotropic state is stable. In the asymptotic limit $a/L \gg 1$ and $b/L \gg 1$, the confined system modeled here reduces back to this transition as the boundary effects diminish.

B. Nematic patterns, when $L^2\rho = 10$

Here we consider the case of $L^2\rho = 10$, which places the system inside a relatively strong nematic state. Beyond the basic D, X, and L states, the Onsager model yields a number of metastable defect states that are of interesting properties. A compilation of these states are shown in Figs. 3 and 4. Figure 5(a) is a phase diagram in terms of $[a/b, a/L]$, when $L^2\rho$ is fixed at 10.

The color in Fig. 5 illustrates the relative probability between two compared states A and B, following the Boltzmann distribution function, $P_A/P_B = \exp[-\beta(F_A - F_B)]$, where βF is the reduced free energy of the system. Given all possible initial conditions, or, if the system can be thermally equilibrated, this directly represents the relative probability of finding state A over state B. However, the free-energy barrier between low- and high-probability states can be so high that a low-probability state can be kinetically trapped when the experimental condition (or the theoretical initial guess) prepares the system in such a state. The shaded areas in these diagram show the parameter space where the metastable states can be found. To find these areas, we prepared the initial guess by a suitable ansatz function.

The diagonal state (D), shown in Figs. 3(a) and 4(a), is one of the most basic and most-studied defect patterns for all ratios of a/L. It has the lowest free energy over a large parameter space shown in Fig. 5(a), as the major body of the structure has a single nematic domain. Galanis *et al.* [5] described this nematic pattern in centimeter-long granular rods confined by a square cell of 29-cm diagonal size, experimentally; the structure was visualized by their digital images [5], and one of them is reproduced here as Fig. 6(a). Tsakonas *et al.* [1] reported the light transmission intensity observed by placing a thermotropic liquid crystal, E7, in micron-sized square cells between crossed polarizers [1]. The light intensity images, $I_{\pi/4}$,

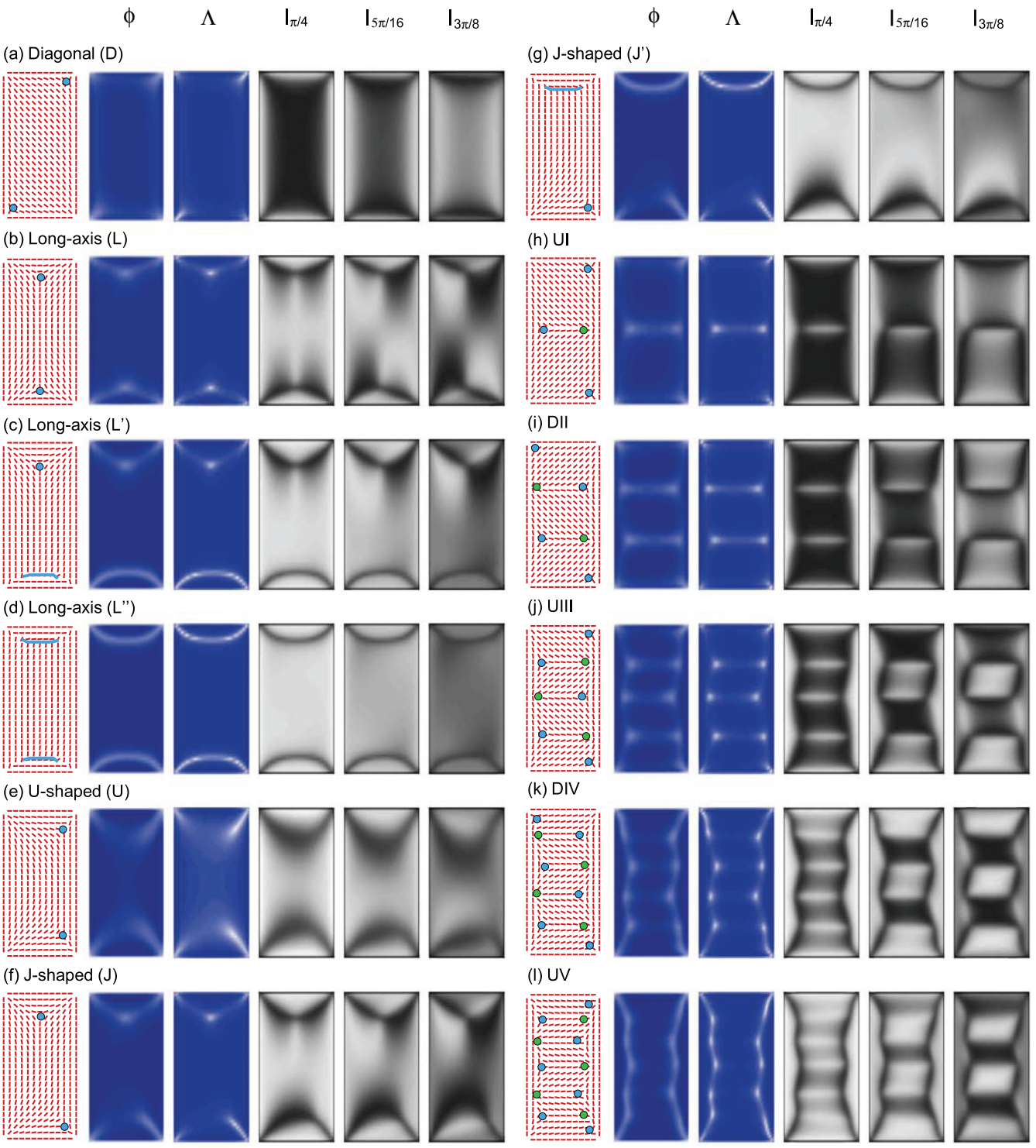

FIG. 4. Nematic defect structures found from the solutions to the extended Onsager model for a rectangular box of aspect ratio $b/a = 2$. Every structure is visualized by six methods: nematic director field, nematic fluid density variation ϕ, main-axis orientational order parameter Λ, and three gray-scale crossed-polarizer images calculated according to (10) for $\alpha = \pi/4$, $5\pi/16$, and $3\pi/8$. The system parameters used to produce these structures are $[L^2\rho, a/L] = [10.0, 7.5]$ for (a), $[8.0, 6.0]$ for (e), and $[10.0, 10.0]$ for (b)–(d) and (f)–(l). The color and grayscales and the meaning of colored circles are the same as in Fig. 3.

$I_{5\pi/16}$, and $I_{3\pi/8}$, constructed from our numerical results and displayed in Fig. 3 are nearly identical to the experimental images, hence indirectly confirming that their observed state is D, a conclusion also supported by their own solutions to the Landau–de Gennes model.

Soares e Silva *et al.* [2] imaged the florescence filaments embedded in 6-μm-long actin filaments confined by a square cell of 30-μm side length [Fig. 6(b)], which also displays the same orientational pattern [2]. D is the common state that appears in the square-confinement solutions of the Landau–de

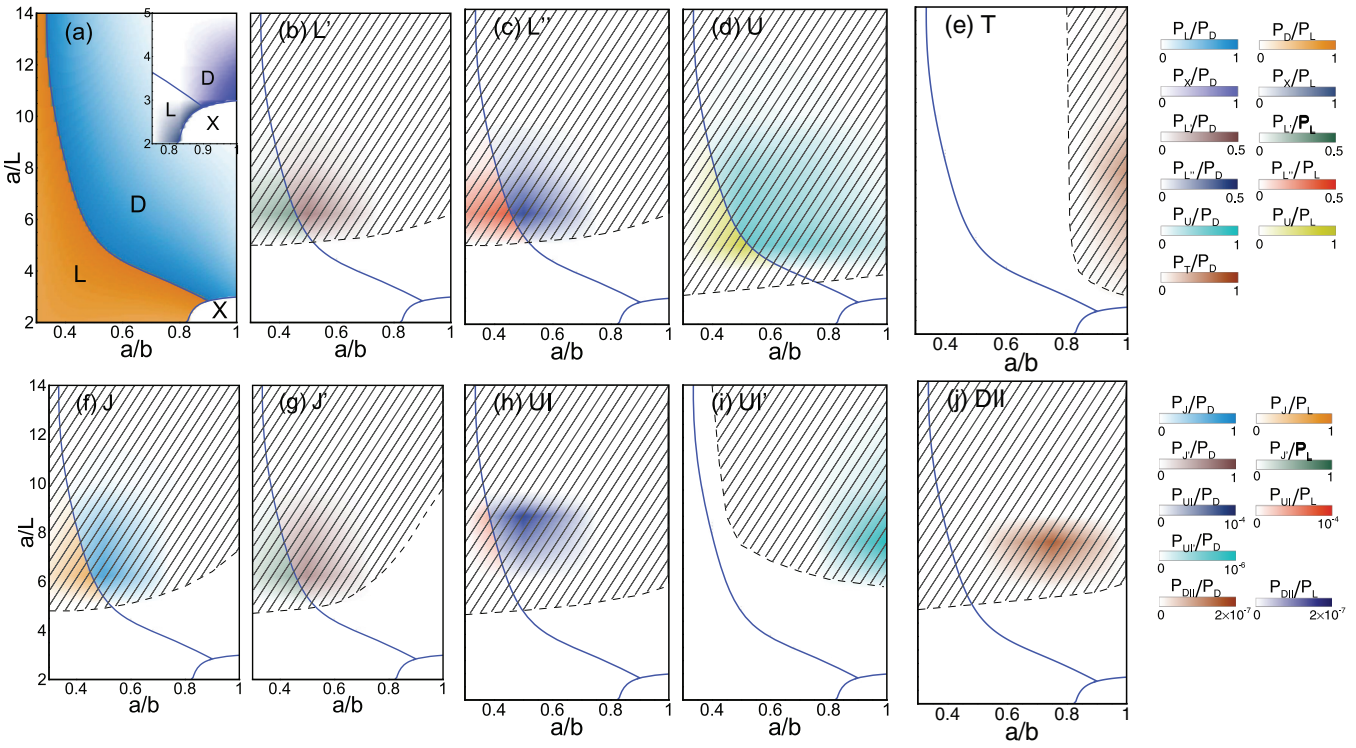

FIG. 5. Phase diagram and the probabilities for appearance of metastable states, P, in the nematic phase for a given $L^2\rho = 10$. The solid phase boundary in all plots divides D, L, and X states. The shaded areas are metastable regions. The color bars specify the relative probabilities, in comparison with those in states D and L.

Gennes theory [1,30,31] and the extended Onsager theory [24], the Monte Carlo simulations of rodlike particles in a slit with a square-boundary [28,30], and the rectangle-confinement solution of the Oseen-Frank theory [3]; these patterns are reproduced here as Figs. 6(c)–6(f), respectively. The same D state was observed in Y21M and *fd-wt*-viruses confined in a flat rectangular box [3]; one example image is reproduced here as Fig. 6(g).

In a system with relatively small a/L, the boundary effects are more profound, influencing the structures in the box interior. When the box is nearly square ($b/a - 1 \lesssim 0.2$), a structure that keeps the four-sided symmetry of the original box, the X-shaped (X) pattern, is stable according to the inset of the phase diagram in Fig. 5(a). X has a single defect point at the center of the box and its main properties are illustrated by Fig. 3(b). It was deemed metastable previously from the preliminary solution of the extended Onsager model in a square box [24]; however, it is found here stable in a small parameter region. Robinson *et al.*'s recent solution to the Landau–de Gennes model analyzes the stability of X, too [30]. Most experimental systems taken so far fall outside of the parameter region; it would be useful to verify the prediction for the existence of the X-state experimentally.

Another stable structure where the symmetry is inherited from the box boundary condition is the long-axis state, L, where the main domain of the nematic structure aligns with the long box-side direction, shown in Fig. 4(b). It is one of the basic structures where a twofold symmetry is maintained, naturally occurring for a system of large aspect ratio b/a, as described by the phase diagram in Fig. 5(a). Lewis *et al.* [3] reported the existence of L in Y21M and *fd-wt* viruses confined by a rectangle with a large b/a, experimentally, showing an image of the dominating, long-axis nematics [see Fig. 6(h)]; they regarded that as a uniform nematic state. On the other hand, a careful examination of that image gives a hint of tilted nematic directions near the two ends of the narrow box; the image is similar to the director field produced from our solution shown in Fig. 6(i) where the two defect points are located near the ends of the rectangular box, which were, within good possibility, poorly captured by their experiment.

Less intuitively, our work predicts that L can be found, although metastable, for a confining square box $b/a = 1$ [see Fig. 3(c)], which was conceptually suggested as a possibility without proof in Ref. [24]. The spatial symmetry of L is closely related to those of L′ and L″, shown in Figs. 3(d) and 3(e), where the latter contain defect lines. They are recently found as the solutions to the Landau–de Gennes model as well [30]. These three can coexist in the same parameter region but L′ and L″ are much less stable, according to the assessment in Figs. 5(b) and 5(c). Coincidentally, using the Zwanzig model [37] (which oversimplifies a nematic structure by forcing rodlike particles to align only in the x and y directions and hence renders D impossible), González-Pinto *et al.* reported that L″ is stable [38]. Cortes *et al.* [4] reported a confocal-microscopy nematic image of confined colloidal silica rods of 4 to 5 μm length in a $a/L = 15$ square box [reproduced as Fig. 6(j)]. According to Fig. 5(a), in the region near $a/L \sim 15$, the relative probability for natural occurrence of L, in comparison with that of D, is low. On the other hand, their nematic state is clearly trapped in the L state with two

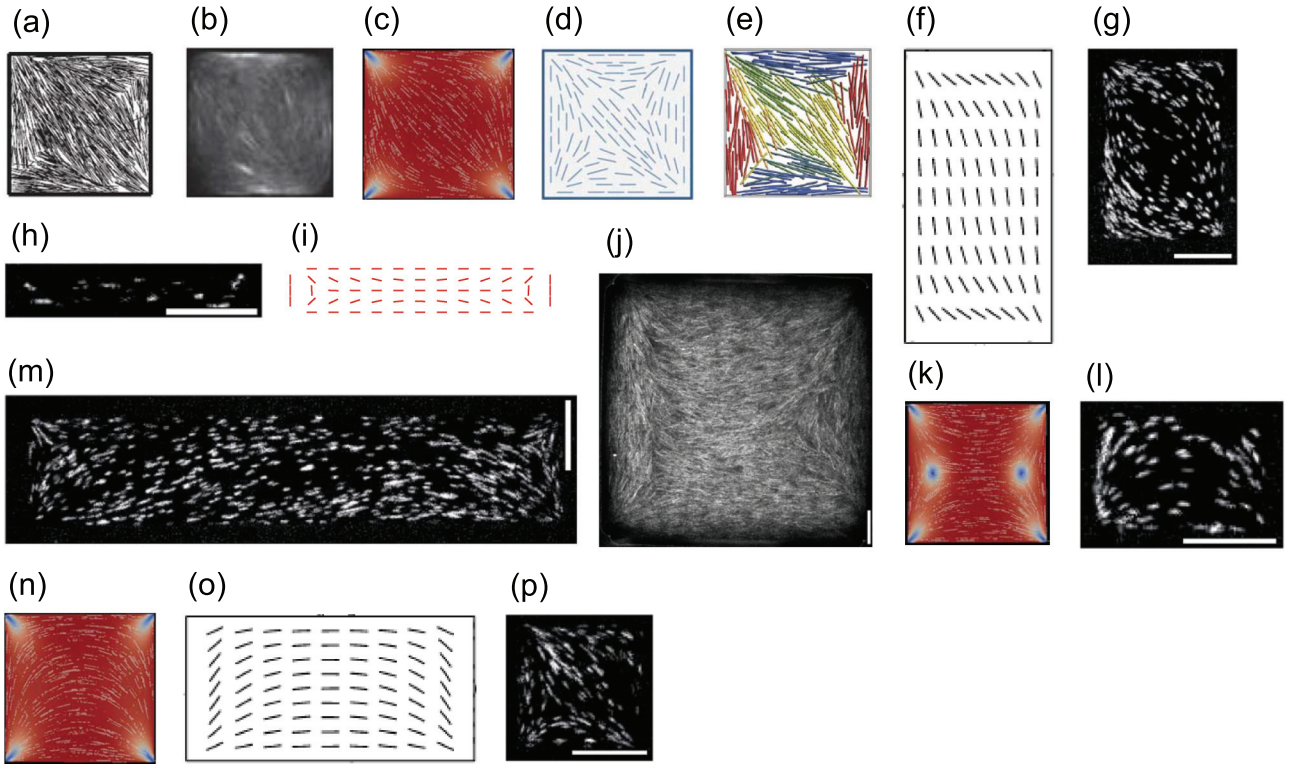

FIG. 6. Comparison to nematic textures found experimentally and theoretically. These plots are adapted from (a) Ref. [5] (experiment on granular rods); (b) Ref. [2] (experiment on actin filaments); (c), (k), and (n) Ref. [30] (solution to LdG model); (d) Ref. [24] (solution to the Onsager model); (e) Ref. [28] (MC simulations); (f) and (o) Ref. [3] (solution to the Oseen-Frank model); (g), (h), (l), (m), and (p) Ref. [3] (experiment on Y21M and *fd-wt* viruses); as well as (j) Ref. [4] (experiment on colloidal rods). All plots were reproduced with consents from the original authors. Systems in (a)–(g) are in the D state, (h)–(k) L state, (l)–(o) U state, and (p) T state. More images have been published in Ref. [3]; the most characteristically representative ones are reproduced here.

defect points, similar to our illustration in Fig. 3(c). It should be realized that in their experiment, they started from a dense, smectic-*A* state with the nematic director aligned along a box side; all L, L′, and L″ (not D) are closely related intermediate states on the pathway to an isotropic state. Because of the special initial condition, L can be energetically separated from the ground D state that would require the rotation of the main orientational axis. This comes as the concrete experimental validation of the existence of L for a $b/a = 1$ system.

We find four other metastable structures in all parameter regions searched: U, T, J, and J′. The structure with a U-shaped (U) bending nematic domain [Figs. 3(f) and 4(e)] occupies almost the entire phase diagram, except for the low a/L region, as illustrated by the shaded area in Fig. 5(d). It has no rotational symmetry but contains a mirror symmetry. Tsakonas *et al.* [1] observed a typical image of U when they placed square wells filled with E7 liquid crystals between crossed polarizers. Our simulated images, $I_{\pi/4}$, $I_{5\pi/16}$, and $I_{3\pi/8}$ in Fig. 3(f) for U, are almost identical to the three plots in the middle column of their Fig. 2. Tsakonas *et al.* [1] claimed that D and U are energetically degenerate. This cannot be the case, as the free energies associated with these two different patterns should be different; qualitatively, placing two same-signed defects at a shorter distance in U is bound to increase its free energy. The metastability of U was well documented by Lewis *et al.* [3] when they produced multiple virus systems confined by rectangles with various values of a/L [3] [Figs. 6(l) and 6(m)] experimentally. There is a close agreement between the probabilities of finding U assessed there and our Fig. 5(d). Theoretically, U has been found in the square-confinement solutions of the Landau–de Gennes theory [1,30,31] and the rectangle-confinement solution of the Oseen-Frank theory [3] [reproduced as Figs. 6(n) and 6(o)].

Here we discover a tilted-T (T) state shown in Fig. 3(g). It displays two nematic defect points, one close to the square center and the other on a diagonal line near a corner. In T, a diagonal symmetry is maintained. The structure can be typically found in a near-square confining box, as illustrated in Fig. 5(e), due to the embedded symmetry. Experimentally, Lewis *et al.* reported a nematic pattern that clearly resembles T [see reproduced Fig. 6(p)], when they confined Y21M and *fd-wt* viruses in a near-square box, which they identified as a variation of the D state [3].

Both J and J′ are metastable low-symmetry solutions, which were reported as recent solutions to the Landau–de Gennes model as well [30]. These states have not been observed experimentally yet but, according to our assessment of the phase diagram, Figs. 5(f) and 5(g), they could be easily found.

C. Nematic patterns, when $L^2\rho = 6$

The parameter regions explored in the last subsection correspond to systems having relatively strong nematic ordering. As

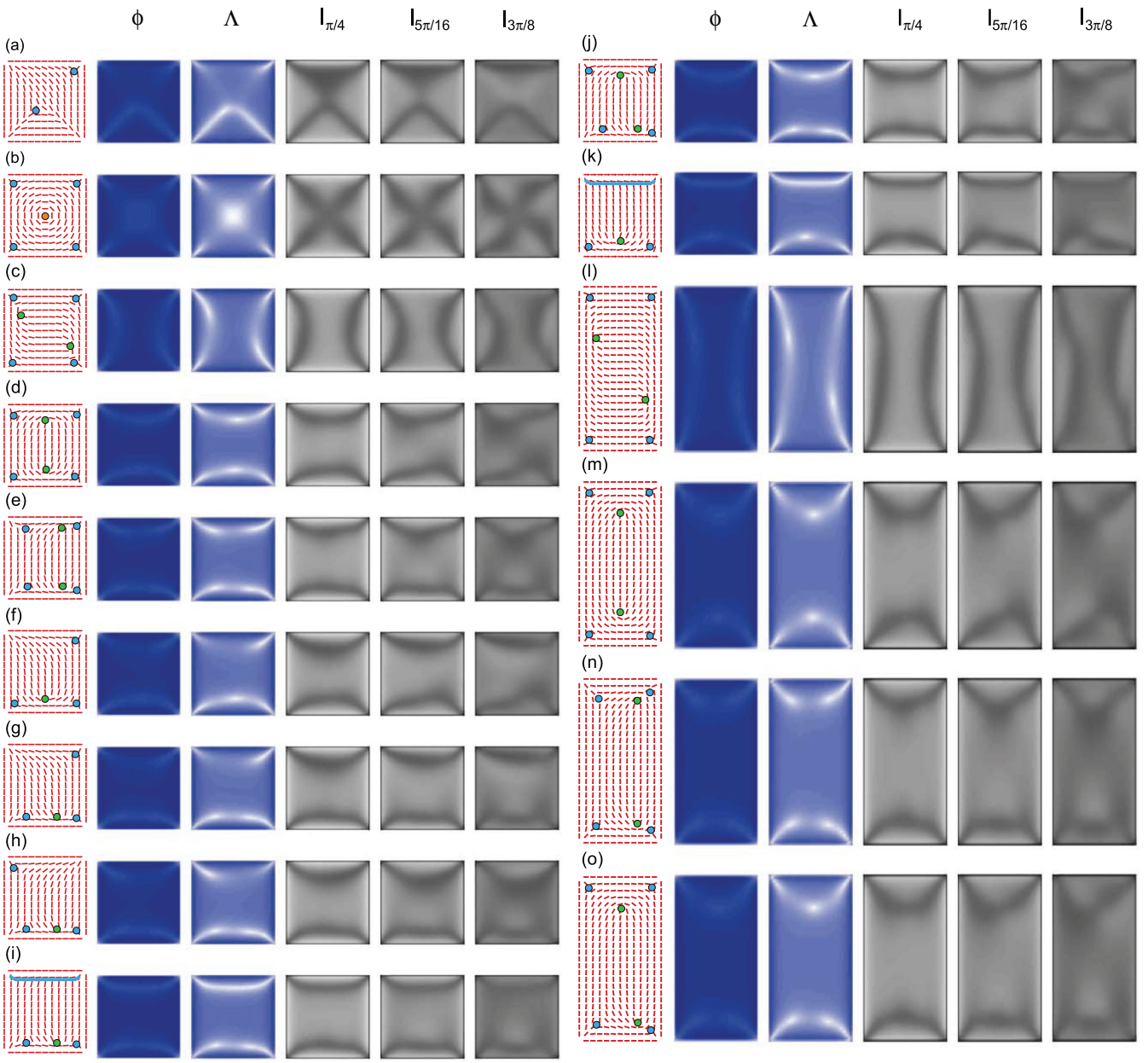

FIG. 7. Additional nematic defect structures found from the solutions to the extended Onsager model for $b/a = 1$ and $b/a = 2$. See the caption of Fig. 3 for an explanation of the physical quantities illustrated. The reduced parameters used to produce these structures are $[L^2\rho, a/L] = [6.0, 12.5]$. The color and grayscales, as well as the meaning of the colored circles, are the same as in Fig. 3. In addition, the orange circle labels the defect location of a defect of the $+1$ winding number.

such, the splay elastic modulus is expected to be much larger than the bending elastic modulus. To solve a typical Landau–de Gennes model [1,30,31], on the other hand, one would customarily equate these two elastic constants; Robinson *et al.* [30] reported many other metastable states on the basis of this approximation [30]. It is perhaps not accidental that experimental observations are only D, L, U, and T, as most experiments are conducted in the strong nematic regime.

We directly use excluded-volume based interaction energy in this work, which avoids the pitfall of a single elastic modulus. In this subsection, we explore an interesting area of the parameter space by letting $L^2\rho = 6$, which is a density right above the isotropic-nematic transition density in (11). As generally expected, near the transition point, the two elastic constants are of the same order. We see below that the extended Onsager model gives rise to a large variety of defect patterns, some reproducing those in Ref. [30].

Figure 7 lists these defect states, found at $[L^2\rho, a/L] = [6.0, 12.5]$ for the cases $b/a = 1$ and $b/a = 2$. They all display the essential features that follow the general principles of nematic defects. For example, regardless of the number of excited defect points, the total sum of winding number is fixed at -1. The positioning of defects having positive and negative winding numbers approximately follows the electrostatic-interaction comparison. We decide not to name these structures because of the richness of the excited defect patterns. Some of

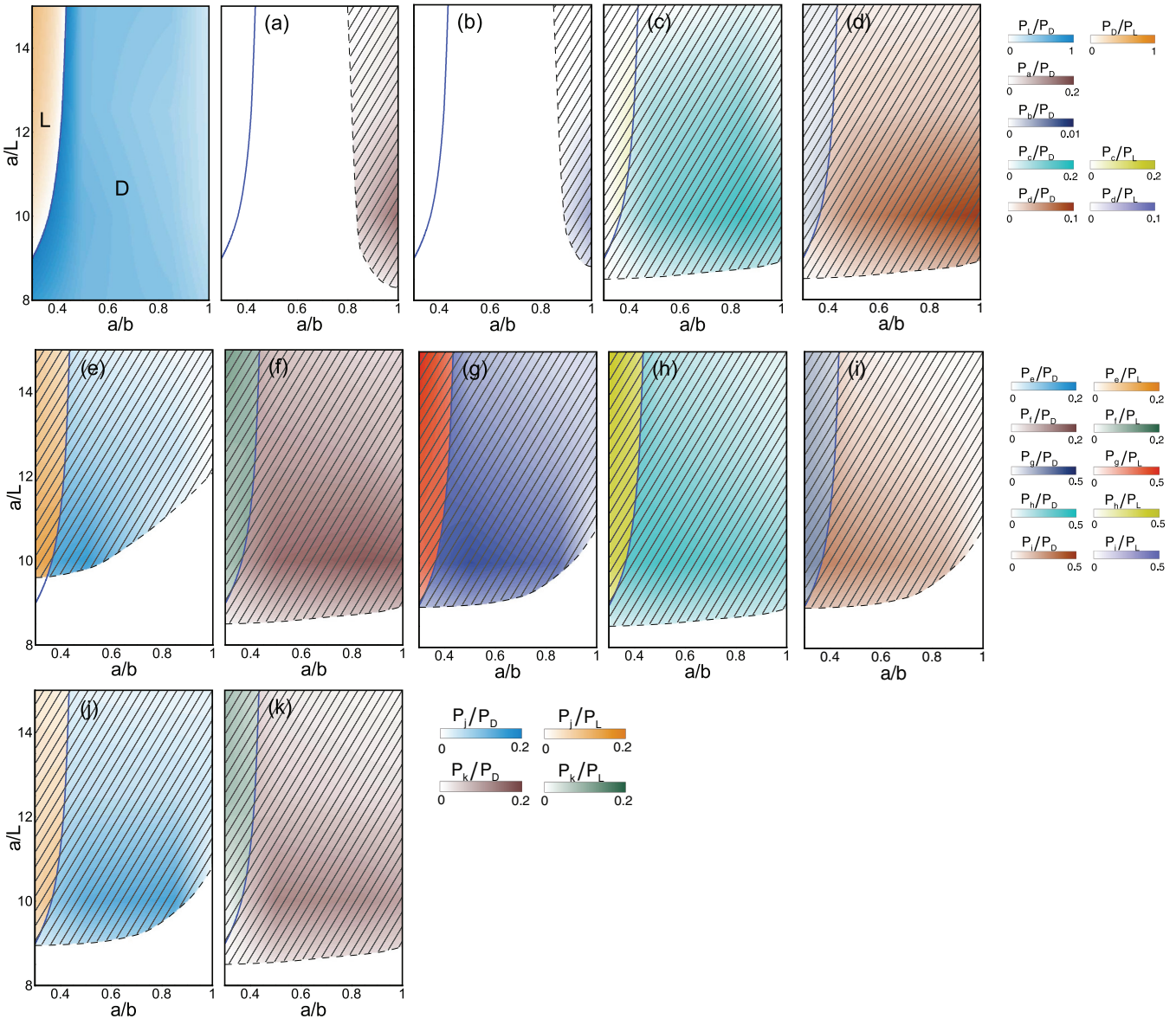

FIG. 8. Phase diagram and the probabilities for appearance of metastable states, P, in the nematic phase (for a given $L^2\rho = 6$). The solid phase boundary in all plots divides the D and L states. The shaded areas in plots (a)–(k) represent the metastable regions of the structures listed in Fig. 7. The color bars specify the relative probabilities, in comparison with those in states D and L.

them can be related to a $\pm 1/2$-pair insertion into the basic structures described in Figs. 3 and 4.

In total, within the parameter regimes considered, we have found 23 defect structures for the case of square confining box, $b/a = 1$. Most of them could also exist when the confining square box becomes rectangular. One important contribution of the current work is the assessment of the stability region and comparative probability of various states. Most basic structures in Fig. 3 have large parameter regimes of stability with well-defined nematic ordering. Deep in the nematic states, the metastable states can be partitioned from the energetically preferred ground states, hence in many cases, they become experimentally observable. This can be contrasted with the stability regimes described in Fig. 8. These more exotic defect states appear to have similar free energies as those of L and D. In a real system near the isotropic-nematic transition point, large local density fluctuations exit and that can easily open up kinetic pathways to the ground states. The question of whether these excited defect states can be found experimentally in real systems or in computer simulations containing molecular details remains.

D. Line boundaries and defects

According to the general theory of nematic defect structures [39–42], the total winding number as the summation of individual contributions, must be the same for a given type of geometric frustrations. The hard-wall boundary condition adopted in this work yields the tangential boundary condition (planar alignment), which enforces the main molecular axis to align in parallel to the confining wall surface perfectly [43,44]. One can measure this total winding number by taking

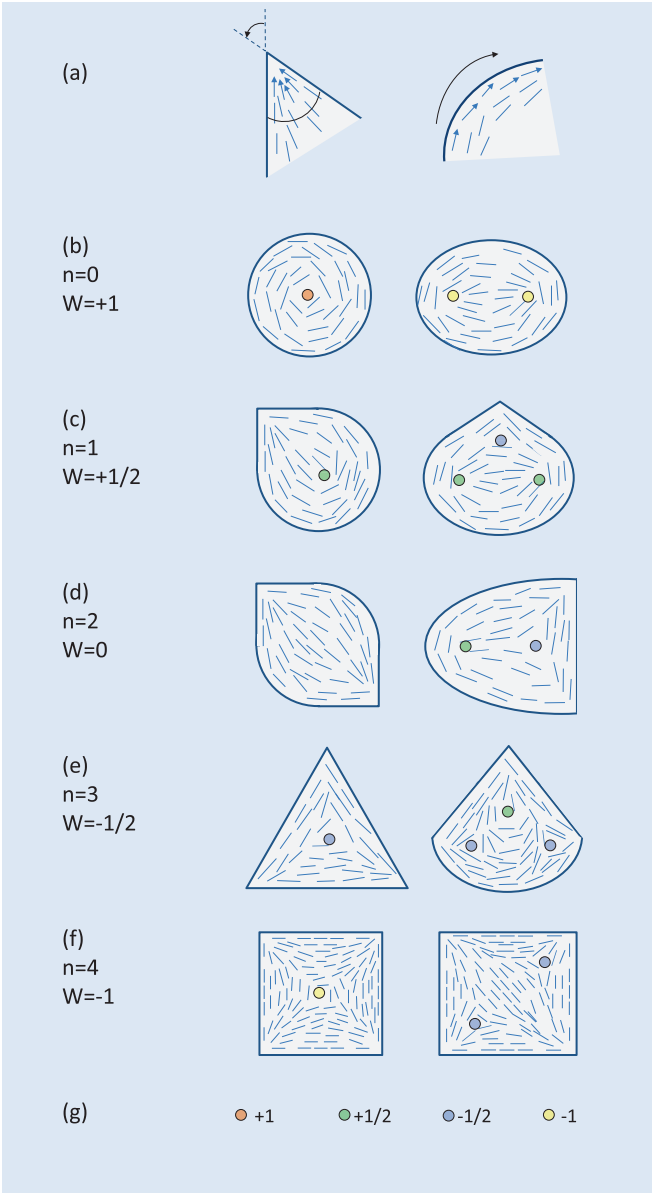

FIG. 9. (a) Winding angle of a sharp angle boundary (left) and a smooth boundary (right), (b)–(f) the total winding numbers of different types of boundary geometries, and (g) the types of defect points labeled by their winding numbers. Every type of frustrations is represented by the total number of corners along the boundary, n. Two example defect patterns of the same total winding number are shown for each case.

a complete loop along the wall boundary and tracing the angular rotation of a unit vector after the completion of the loop.

Figure 9(a) shows two possible geometry boundaries that such a loop can encounter. Following the change of molecular directions inside the corner (labeled by arrows for clarity), the boundary corner of angle α produces a rotation of $-\alpha$ of the director field. In comparison, a smooth boundary of radial angle α produces a $+\alpha$ change. Adding all contributions, we found that the total winding angle is simply the the negative sum of all internal angles after mapping a closed boundary (which might contain curve segments) into a polygon consisting of straight lines only.

Then we can establish a simple rule of the total winding number. According the geometry theory, the total sum of internal angles is $(n-2)\pi$ for a polygon consisting of n corners. Hence the total winding number is

$$W(n) = -(n-2)\pi/2\pi = -(n-2)/2. \tag{12}$$

As far as we are aware of, this rule has not been made explicit in the literature of liquid crystal defects for a 2D confinement shape made of acute and obtuse angles.

Figures 9(b)–9(f) illustrate simple examples that follow this rule. In particular, for rectangular confinement, $n = 4$, the total winding number is -1. This is indeed satisfied by all defect patterns, in Figs. 3, 4, and 7.

When the argument is generalized to other closed line boundaries, interesting defect patterns can be guessed. For example, along a the circular (or elliptical) confinement boundary, $n = 0$ and hence $W = +1$. The two example patterns shown in Fig. 9(b) were the defect patterns produced from solving the extended Onsager model [24] and the second one was observed experimentally [2,5]. This smooth-edged boundary has the same topology as a spherical surface, on which the total winding number is known to follow the Poincaré-Hopf theorem [45].

The first pattern of a liquid crystal confined inside a triangle, Fig. 9(e), agrees with the experimental observation of the same type [2]. The other patterns in Figs. 9(c)–9(e) are demonstrated here for the first time.

Our general formula, (12), depends on the assumption that nematic texture at a corner has a splay pattern [left panel of Fig. 9(a)], not a bending pattern [right panel of Fig. 9(a)]. In some previous theoretical work, however, soft boundary conditions were used where the nematic layers at the boundaries are allowed to point at directions other than planer, with an energy penalty. One consequence is that the near-corner defects can resolve themselves to save the local defect-point free energy at the expense of increasing the energy penalty of the nearby boundary molecules, which are now tilted from the perfect planar condition [1,3,31]. For example, the nematic defects seem to have melted away at the rectangular corners of plots in Figs. 6(f) and 6(o), which can be contrasted with the defects showing in our Figs. 3 and 4. In these soft boundary cases, the tilted boundary molecules do not follow the analysis schematically presented in the left panel of Fig. 9(a). As such, the formula in (12) can no longer be followed.

In a recent study of the Landau–de Gennes model, the Dirichlet planar boundary condition seems to be followed on most line boundaries [30]. The corner point itself is a singularity for perfect boundary conditions in that treatment. There is a very small area at the corners of some illustrations where it neighbors a corner and a bending nematic texture rather than a corner and splay nematic texture. The finite anchoring strength used in that work to simulate the Dirichlet boundary condition would make a bend distortion at the corner admissible.

Our numerical work also demonstrates that when a $-1/2$ defect point is located very close to a corner to form a $-1/2$-defect-corner pattern, the region containing the defect and the corner is associated with a depletion of the molecular density

(ϕ plots in Figs. 3, 4, and 7). In real experimental systems, the depletion directly lowers the intensity on an optical image. This perhaps is the reason why the $-1/2$-defect-corner pattern is not always explicitly visible on optical images in Refs. [2,28].

To summarize, here we show that a general defect rule, (12), is mathematical exact when liquid crystals are confined by a planar line boundary condition for classification purposes. We also discussed a few scenarios when (12) is apparently violated. Assessment of those nematic textures with seemingly disappeared defects in $-1/2$-defect-corner regions should be augmented by $-1/2$ defects to void confusion in classification.

E. Excited states

Our calculation shows that excited states beyond basic structures can be stabilized. For example, pairs of $\pm 1/2$ defects are inserted into the basic defect patterns. Among these are UI [Figs. 3(j) and 4(h)] and its variation UI′ [Fig. 3(k)], UIII [Fig. 4(j)], and UV [Fig. 4(l)], where one, three, and five $\pm 1/2$ pairs show up in an otherwise U state, and DII [Figs. 3(l) and 4(i)] and DIV [Fig. 4(k)], where two and four $\pm 1/2$ pairs show up in an otherwise D state. The insertion makes the structure multilayered. Each layer has its own tilted, main nematic direction, altered layer by layer. These structures were found by enforcing the corresponding initial guesses, which traps the systems in these structures during the convergence to the final solutions. The metastable patterns can be created as long as the b/a ratio can accommodate the space needed to sustain the layered structures. As a general guideline, from our trial-and-error, we found that a maximum of three layers can be stabilized per unit b/a. Figures 5(h), 5(i) and 5(j) demonstrate the region in phase space where UI, UI′, and DII can be stabilized. No experimental study yields these excited states so far.

The interaction between nematic defects appearing on a surface can be compared with electrostatics [39,46]. Within this analogy, the defects with a positive (or negative) winding number play the role of a positive (or negative) pointlike charge. Hence, the three repelling negative defects keep themselves as far as possible in UI and the positive defect finds itself a suitable balancing position inside the three negative defects to maximize the attractions it experiences. These excited states can be viewed as insertion of (long) dipole pairs into an existing defect pattern. The alternation of the dipole axes is needed to maintain the electrostatic stability.

Another important fact that must be noted is that the locations of the nematic defects can fluctuate to large extent, as shown by recent molecular simulations [47] and a real-time experimental movie of a colloidal liquid crystal [4]. The current study is mean-field based and produces nematic patterns with particular symmetries. These symmetries may not always be clearly visible in computer simulations or real experiments with fluctuating defects.

IV. SUMMARY

In summary, we examine the 2D nematic-defect structures of rodlike molecules confined in rectangular boxes of various sizes and aspect ratios, using an extended version of the classical Onsager model for liquid crystal systems. The main conclusions are based on numerical solutions to the model, which display a variety of basic and excited defect patterns, all topologically different. All optical images of real experimental systems taken in recent years are now systematically accounted for by our theoretical results. In addition, some structures predicted in this work should be verifiable in further experimental work. The phenomena described here land on a number of branches in physics, materials science, and mathematics, forming problems of fundamental importance.

We have left behind the thread of other technical issues such as whether there is indeed a long-range order in a 2D system [48,49] and whether a density-functional theory [25] can repair the underestimate of the isotropic-nematic transition point from the 2D Onsager model. The current work demonstrates the beauty and triumphs of a fundamental physical idea proposed by Onsager nearly 70 years ago—the directional ordering seen in nematics can be captured by the needs to increase the orientational entropy and to decrease the excluded-volume interaction. While this concept was proposed to deal with the bulk isotropic-nematic transition, addition of the geometric frustrations gives the model a new life. It can be used to study the nematics of rigid molecules embedded on the spherical surface where the topological frustrations of accommodating a headless vector nematic field on a curved closed surface produce multiple nematic defect states [50–52]. It can also be used to study the 2D nematics of rigid molecules frustrated by confining geometry of various shapes: rectangle (this work and Ref. [24]) and circle (Ref. [24]).

While this paper discusses the nematic states found based on a three-parameter model using a/b, a/L, and $L^2\rho$, further extensions could be made to address other aspects of related systems. For example, the diameter of a rod, d, does not enter into the current theory but could be introduced explicitly through the shape of end-caps of rods [12]. The main effects would be the ability of the further extended theory to handel smectic ordering, as shown previously in Ref. [53], in order to tackle, for example, the isotropic-nematic-smectic coexisting problem in a recent experiment [4]. Another interesting direction of extension of the current work would be to consider semiflexible chains rather than rigid rods, as "molecules" in most biological experiments are not exactly rigid. This extension is already built into the self-consistent field theory by using a finite persistence length λ [34]. The introduction of these effects would make the theory depend on a/b, a/L, $L^2\rho$, d/L, and λ/L, resulting a much larger parameter space to explore.

The formation of the nematic ordering predicted from the Onsager theory is density driven. Strictly speaking, the theory only describes "lyotropic" systems to which most of the experiments described here belong. The liquid crystal system in Ref. [1], however, more likely belongs to another class, "thermotropic" liquid crystals. The basic natures, such as boundary frustrations against uniform nematic ordering, are the same in both confined thermotropic and lyotropic systems. As long as a thermotropic liquid crystals is brought into a nematic state (by temperature change), the defect patterns discussed in the present work (generated by density change) should also be qualitatively applicable.

ACKNOWLEDGMENTS

The authors acknowledge financial support from the National Science Foundation of China (Grants No. NSFC-11471046 and No. NSFC-11571045) and the Natural Sciences and Engineering Council of Canada.

APPENDIX A: SELF-CONSISTENT FIELD THEORY

The extended Onsager model presented in the text,

$$\beta F = \int \rho_c(\mathbf{r},\mathbf{u}) \ln[L^2 \rho_c(\mathbf{r},\mathbf{u})] d\mathbf{r} d\mathbf{u} + \frac{1}{2} \int \rho_c(\mathbf{r},\mathbf{u}) w(\mathbf{r},\mathbf{u};\mathbf{r}',\mathbf{u}') \rho_c(\mathbf{r}',\mathbf{u}')\, d\mathbf{r} d\mathbf{u} d\mathbf{r}' d\mathbf{u}', \tag{A1}$$

can be reformulated as a self-consistent field theory (SCFT) for wormlike polymers with an infinitely large persistence length (hence the molecules are rigid), which is summarized here. The proof for mathematical equivalence is carefully addressed in both Refs. [24] and [34]. The formalism requires the introduction of a path variable s, continuously varying from one end of the molecule where $s = 0$ to another end where $s = 1$. The direction of the unit vector $\mathbf{u}$ is assumed to point from $s = 0$ to 1. A segment element on the rodlike molecule then carries a label s.

A few advantages can be gained by using the path-averaged distribution function within the SCFT, $f(\mathbf{r},\mathbf{u})$. The second *nonlocal* term in (A1) can now be simply written with a local kernel function without the complex structure of w; the *nonlocal* boundary conditions at the walls can be handled through the *local* boundary conditions of the reduced Green's function. The price that must be paid for these simpler expressions is the more complicated entropy term. Instead of the *local* expression shown in the first term of (A1), in terms of $f(\mathbf{r},\mathbf{u})$ a *nonlocal* relationship now needs to be considered, which, within SCFT, is determined by the solution to a partial differential equation.

The density function is related to the reduced Green's function $q(\mathbf{r},\mathbf{u};s)$ by

$$f(\mathbf{r},\mathbf{u}) = \frac{n}{\rho Q} \int_0^1 ds q(\mathbf{r},\mathbf{u};s) q(\mathbf{r},-\mathbf{u};1-s), \tag{A2}$$

where Q is the single-chain partition function,

$$Q = \int d\mathbf{r} d\mathbf{u} q(\mathbf{r},\mathbf{u};1). \tag{A3}$$

The reduced Green's function $q(\mathbf{r},\mathbf{u};s)$ is introduced to describe the probability of finding a polymer segment of length s with its terminal end locating at $\mathbf{r}$ and pointing at unit vector $\mathbf{u}$. Given an external potential $W(\mathbf{r},\mathbf{u})$, $q(\mathbf{r},\mathbf{u};s)$ can be calculated by solving the modified diffusion equation (MDE) [24]

$$\frac{\partial}{\partial s} q(\mathbf{r},\mathbf{u};s) = \left[(L/2\lambda)\nabla_{\mathbf{u}}^2 - L\mathbf{u}\cdot\nabla_{\mathbf{r}} - W(\mathbf{r},\mathbf{u})\right] q(\mathbf{r},\mathbf{u};s), \tag{A4}$$

where an initial condition $q(\mathbf{r},\mathbf{u};s=0) = 1$ is imposed. In this work we already assume that the persistence length of the polymer $\lambda \gg L$ to model a rodlike polymer.

The free energy in the extended Onsager model can be rewritten as

$$\beta F = n \ln(\rho/Q) - \rho \int d\mathbf{r} d\mathbf{u} W(\mathbf{r},\mathbf{u}) f(\mathbf{r},\mathbf{u}) + \frac{L^2\rho^2}{2} \int d\mathbf{r} d\mathbf{u} d\mathbf{u}' f(\mathbf{r},\mathbf{u}) |\mathbf{u}\times\mathbf{u}'| f(\mathbf{r},\mathbf{u}'). \tag{A5}$$

The minimization of (A5) with respect to $f(\mathbf{r},\mathbf{u})$, $\delta(\beta F)/\delta f = 0$, gives

$$W(\mathbf{r},\mathbf{u}) = L^2 \rho \int d\mathbf{u}' |\mathbf{u}\times\mathbf{u}'| f(\mathbf{r},\mathbf{u}'), \tag{A6}$$

which relates the mean field W with the distribution function.

The main algorithm of the self-consistent loop is the following. (A) The excluded-volume interaction of the system is modeled by the *local* expression, (A6). (B) For a single-chain statistics, W is considered as an external field and the reduced Green's function problem is solved through (A4), which yields the single-chain partition function through (A3) and probability distribution through (A2). (C) One then goes back to (A6) to complete the self consistency.

APPENDIX B: BOUNDARY CONDITIONS

One of the main constraints that need to be implemented beyond the original Onsager model is the hard-wall potential acting on the molecules [18,22,23,44]. The wall-excluding potential can be easily handled by the use of the q function [24,44]. We let

$$q(\mathbf{r},\mathbf{u};s) = 0 \quad (\text{if } \mathbf{u}\cdot\mathbf{n} \geqslant 0 \text{ and } s \neq 0), \tag{B1}$$

where $\mathbf{n}$ is the normal direction of a wall area element, pointing to the box interior. The other half of function at the wall, for the parameter region $\mathbf{u}\cdot\mathbf{n} < 0$, is specified automatically by the physical problem. The physical significance of this boundary condition, together with the consideration of the mathematical requirements in solving a partial differential equation within a hard wall, is discussed in depth in Sec. 2.5 of Ref. [34].

APPENDIX C: NUMERICAL ALGORITHM TO SOLVE MDE

The center of the numerical calculation is to solve MDE in (A4). In this work we specify $\mathbf{r}$ through 2D variables x, y, and $\mathbf{u}$ through the angle θ that it makes with the x axis. Then the MDE can be represented by

$$\frac{\partial}{\partial s} q(x,y,\theta;s) = \left[-L\cos\theta\frac{\partial}{\partial x} - L\sin\theta\frac{\partial}{\partial y} - W(x,y,\theta)\right] q(x,y,\theta;s), \tag{C1}$$

with the initial condition

$$q(x,y,\theta;0) = 1. \tag{C2}$$

For numerical implementation, we assume that the parameter spaces in x/L, y/L, θ, and s are divided into N_x, N_y, N_θ, and

N_s representative divisions; the nodes are labeled by integers i, j, k, and n. The function $q(x_i, y_j, \theta_k; s_n)$ is then directly represented by $q^n_{i,j,k}$. In most calculations, when $b/a = 1$, we set $(N_x, N_y, N_\theta, N_s)$ to (50,50,30,2000). In the large b/a case, N_y/N_x is adjusted accordingly. For example, when $b/a = 2$, $(N_x, N_y, N_\theta, N_s)$ is set to (50,100,30,2000). The step sizes in x, y, θ, and s are $\Delta x = a/(LN_x)$, $\Delta y = b/(LN_y)$, $\Delta\theta = 2\pi/N_\theta$, and $\Delta s = 1/N_s$.

In terms of x and y, the above is a *first-order* convection equation, which can be tackled by using the implicit upwind scheme. We write

$$q^{n+1}_{i,j,k} = q^n_{i,j,k} + \widehat{H}_x q^{n+1}_{i,j,k} + \widehat{H}_y q^{n+1}_{i,j,k} + H_W q^{n+1}_{i,j,k}. \tag{C3}$$

Here $H_W = -\Delta s\, W_{i,j,k}$ and the operators $\widehat{H}_x$ and $\widehat{H}_y$ yield

$$\widehat{H}_x q^{n+1}_{i,j,k} = \begin{cases} -\cos\theta_k \frac{\Delta s}{\Delta x}\left(q^{n+1}_{i,j,k} - q^{n+1}_{i-1,j,k}\right), & \cos\theta_k \geqslant 0 \\ -\cos\theta_k \frac{\Delta s}{\Delta x}\left(q^{n+1}_{i+1,j,k} - q^{n+1}_{i,j,k}\right), & \cos\theta_k < 0 \end{cases}, \tag{C4}$$

$$\widehat{H}_y q^{n+1}_{i,j,k} = \begin{cases} -\sin\theta_k \frac{\Delta s}{\Delta y}\left(q^{n+1}_{i,j,k} - q^{n+1}_{i,j-1,k}\right), & \sin\theta_k \geqslant 0 \\ -\sin\theta_k \frac{\Delta s}{\Delta y}\left(q^{n+1}_{i,j+1,k} - q^{n+1}_{i,j,k}\right), & \sin\theta_k < 0 \end{cases}. \tag{C5}$$

Since the $\partial/\partial s$ operator is treated by Euler's forward scheme, the increment Δs must be small enough to ensure numerical stability to satisfy the Courant-Friedrichs-Lewy condition.

The above equations can be formally represented by the following notation:

$$A\,Q^{n+1} = Q^n, \tag{C6}$$

where we move all linear terms associated with the time step $n+1$ to the left-hand side. The $N_x \times N_y \times N_\theta$-dimensional matrix A contains all coefficients of these terms and is sparse, which can be inverted by using a standard algorithm. The $N_x \times N_y \times N_\theta$-dimensional vector Q^{n+1} representing $q^{n+1}_{i,j,k}$ is then calculated at time step $n+1$ when Q^n is given.

[1] C. Tsakonas, A. J. Davidson, C. V. Brown, and N. J. Mottram, Appl. Phys. Lett. **90**, 111913 (2007).
[2] M. Soares e Silva, J. Alvarado, J. Nguyen, N. Georgoulia, B. M. Mulder, and G. H. Koenderink, Soft Matter **7**, 10631 (2011).
[3] A. H. Lewis, I. Garlea, J. Alvarado, O. J. Dammone, P. D. Howell, A. Majumdar, B. M. Mulder, M. P. Lettinga, G. H. Koenderink, and D. G. A. L. Aarts, Soft Matter **10**, 7865 (2014).
[4] L. B. G. Cortes, Y. Gao, R. P. A. Dullens, and D. G. A. L. Aarts, J. Phys.: Condens. Matter **29**, 064003 (2017).
[5] J. Galanis, D. Harries, D. L. Sackett, W. Losert, and R. Nossal, Phys. Rev. Lett. **96**, 028002 (2006).
[6] J. Galanis, R. Nossal, W. Losert, and D. Harries, Phys. Rev. Lett. **105**, 168001 (2010).
[7] P. G. de Gennes and J. Prost, *The Physics of Liquid Crystals* (Oxford University Press, Oxford, 1993).
[8] H.-R. Trebin, Adv. Phys. **31**, 195 (1982).
[9] M. Kléman, Rep. Prog. Phys. **52**, 555 (1989).
[10] M. Kléman and O. D. Lavrentovich, Philos. Mag. **86**, 4117 (2006).
[11] G. P. Alexander, B. G.-g. Chen, E. A. Matsumoto, and R. D. Kamien, Rev. Mod. Phys. **84**, 497 (2012).
[12] L. Onsager, Ann. N. Y. Acad. Sci. **51**, 627 (1949).
[13] D.-K. Yang and S.-T. Wu, *Fundamentals of Liquid Crystal Devices* (John Wiley & Sons, New York, 2006).
[14] I. Dozov, M. Nobili, and G. Durand, Appl. Phys. Lett. **70**, 1179 (1997).
[15] R. Barberi, J. J. Bovent, M. Giocondo, M. Iovane, and A. L. Alexe-Ionescu, J. Appl. Phys. **84**, 1321 (1998).
[16] S. Kitson and A. Geisow, Appl. Phys. Lett. **80**, 3635 (2002).
[17] W. E. McMullen, Phys. Rev. A **38**, 6384 (1988).
[18] R. Holyst and A. Poniewierski, Phys. Rev. A **38**, 1527 (1988).
[19] B. G. Moore and W. E. McMullen, Phys. Rev. A **42**, 6042 (1990).
[20] Z. Y. Chen and J. Noolandi, Phys. Rev. A **45**, 2389 (1992).
[21] Z. Y. Chen, Phys. Rev. E **47**, 3765 (1993).
[22] D. L. Koch and O. G. Harlen, Macromolecules **32**, 219 (1999).
[23] K. Shundyak and R. van Roij, J. Phys.: Condens. Matter **13**, 4789 (2001).
[24] J. Z. Y. Chen, Soft Matter **9**, 10921 (2013).
[25] D. de las Heras, E. Velasco, and L. Mederos, Phys. Rev. E **79**, 061703 (2009).
[26] J. Dzubiella, M. Schmidt, and H. Löwen, Phys. Rev. E **62**, 5081 (2000).
[27] T. Geigenfeind, S. Rosenzweig, M. Schmidt, and D. de las Heras, J. Chem. Phys. **142**, 174701 (2015).
[28] I. C. Gârlea and B. M. Mulder, Soft Matter **11**, 608 (2015).
[29] I. C. Gârlea, P. Mulder, J. Alvarado, O. Dammone, D. G. A. L. Aarts, M. P. Lettinga, G. H. Koenderink, and B. M. Mulder, Nat. Commun. **7**, 12112 (2016).
[30] M. Robinson, C. Luo, P. E. Farrell, R. Erban, and A. Majumdar, Liq. Cryst. **44**, 2267 (2017).
[31] C. Luo, A. Majumdar, and R. Erban, Phys. Rev. E **85**, 061702 (2012).
[32] R. Pathria, *Statistical Mechanics* (Butterworth Heinemann, Oxford, UK, 1996).
[33] M. Doi, *Soft Matter Physics* (Oxford University Press, New York, 2013).
[34] J. Z. Y. Chen, Prog. Polym. Sci. **54-55**, 3 (2016).
[35] R. F. Kayser and H. J. Raveche, Phys. Rev. A **17**, 2067 (1978).
[36] J. A. Cuesta, C. F. Tejero, and M. Baus, Phys. Rev. A **39**, 6498 (1989).
[37] R. Zwanzig, J. Chem. Phys. **39**, 1714 (1963).
[38] M. González-Pinto, Y. Martínez-Ratón, and E. Velasco, Phys. Rev. E **88**, 032506 (2013).
[39] T. C. Lubensky and J. Prost, J. Phys. II (France) **2**, 371 (1992).
[40] D. R. Nelson, *Defects and Geometry in Condensed Matter Physics* (Cambridge University Press, Cambridge, 2002).
[41] M. J. Bowick and L. Giomi, Adv. Phys. **58**, 449 (2009).
[42] A. M. Turner, V. Vitelli, and D. R. Nelson, Rev. Mod. Phys. **82**, 1301 (2010).
[43] A. Poniewierski and R. Holyst, Phys. Rev. A **38**, 3721 (1988).
[44] Z. Y. Chen and S.-M. Cui, Phys. Rev. E **52**, 3876 (1995).
[45] M. P. Do Carmo, *Differential Geometry of Curves and Surfaces* (Prentice-Hall, Englewood Cliffs, NJ, 1976).

[46] P. M. Chaikin and T. C. Lubensky, *Principles of Condensed Matter Physics* (Cambridge University Press, Cambridge, 1995).
[47] A. Humpert, S. F. Brown, and M. P. Allen, Liq. Cryst. **45**, 59 (2018).
[48] D. Frenkel and R. Eppenga, Phys. Rev. A **31**, 1776 (1985).
[49] M. C. Lagomarsino, M. Dogterom, and M. Dijkstra, J. Chem. Phys. **119**, 3535 (2003).
[50] W.-Y. Zhang, Y. Jiang, and J. Z. Y. Chen, Phys. Rev. Lett. **108**, 057801 (2012).
[51] W.-Y. Zhang, Y. Jiang, and J. Z. Y. Chen, Phys. Rev. E **85**, 061710 (2012).
[52] Q. Liang, S. Ye, P. Zhang, and J. Z. Y. Chen, J. Chem. Phys. **141**, 244901 (2014).
[53] R. C. Hidalgo, D. E. Sullivan, and J. Z. Y. Chen, Phys. Rev. E **71**, 041804 (2005).